Fabrication and manipulation of nanosized graphene homojunction with atomically-controlled boundaries

Hui Chen[1,2,§], De-Liang Bao[1,2,§], Dongfei Wang[1,2], Yande Que[1], Wende Xiao[1], Yu-Yang Zhang[1,2], Jiatao Sun[1,2], Shixuan Du[1,2] (✉), and Hong-Jun Gao[1,2] (✉)

[1] Institute of Physics and University of Chinese Academy of Sciences, Beijing 100190, China
[2] CAS Key Laboratory of Vacuum Physics, University of Chinese Academy of Sciences, Beijing 100049, China
[§] Hui Chen and De-Liang Bao contributed equally to this work.

ABSTRACT

Controlling the atomic configurations of structural defects in graphene nanostructures is crucial for achieving desired functionalities. Here, we report the controlled fabrication of high-quality single-crystal and bicrystal graphene nanoislands (GNI) through a unique top-down etching and post-annealing procedure on a graphite surface. Low-temperature scanning tunneling microscopy (STM) combined with density functional theory calculations reveal that most of grain boundaries (GBs) formed on the bicrystal GNIs are 5-7-5-7 GBs. Two nanodomains separated by a 5-7-5-7 GB are AB stacking and twisted stacking with respect to the underlying graphite substrate and exhibit distinct electronic properties, forming a graphene homojunction. In addition, we construct homojunctions with alternative AB/twisted stacking nanodomains separated by parallel 5-7-5-7 GBs. Remarkably, the stacking orders of homojunctions are manipulated from AB/twist into twist/twist type through a STM tip. The controllable fabrication and manipulation of graphene homojunctions with 5-7-5-7 GBs and distinct stacking orders open an avenue for the construction of GBs-based devices in valleytronics and twistronics.

KEYWORDS

homojunction, graphene nanoislands, manipulations, grain boundaries, twisted stacking

1 Introduction

Graphene nanoislands (GNIs) possess strong quantum confinement and edge effects, which make them excellent materials for constructing nanoscale optical and electronic devices [1–9]. GNIs are readily to be displaced [10], rotated [7] and folded [11, 12] for constructing complex nanostructures with engineered quantum properties and, ultimately, quantum machines [13, 14]. Merging two single-crystal (SC) GNIs into a bicrystal (BC) GNI with specific grain boundaries (GBs) attracts much interest [15], because the BC GNI with specific GBs show distinct valley-polarized transport behaviors [16–18] and unique mechanical [19] or magnetic [20–22] properties, forming a novel graphene homojunction. Furthermore, benefitting from the manipulability of GNIs, the atomic structures of homojunctions can be artificially controlled. However, it has been predicted that the properties of homojunctions rely heavily on the detailed atomic arrangements of GBs. Different from other type GBs, 5-7-5-7 GBs [16] and 5-5-8 GBs [17, 18, 23] show a strong valley polarization. Therefore, controlling the atomic configuration of GBs are crucial for practical applications of GBs-based homojunctions. In experiments, most of GBs formed during the growth of graphene are curved and nonperiodic [24]. Recently, several ordered GBs have been fabricated on epitaxial graphene on SiC(0001) [25] and Cu(111) [26] through optimizing growth conditions. However, controllable fabrication and manipulation of graphene homojunctions with specific GBs

still remain a challenge.

In this work, we report the fabrication of disk-shaped GNIs on highly ordered pyrolytic graphite (HOPG) substrate through a radio frequency (RF) hydrogen plasma etching and thermal post-annealing method. Low-temperature scanning tunneling microscopy/spectroscopy (LT-STM/STS) combined with density functional theory calculations (DFT) show that GBs with a configuration of a periodic alternation of pentagons and heptagons (5-7-5-7 GBs) are widely formed on the as-grown GNIs. The two domains abutting GBs on GNIs, forming a homojunction, are found to be stacked differently with graphite substrate, that is, AB and twist stacking, respectively. In addition, we fabricated homojunctions with alternative AB/twisted stacking nanodomains separated by parallel 5-7-5-7 GBs. Interestingly, using STM-lateral manipulation, we precisely modified the stacking structures of two domains of homojunction.

2 Results and discussion

We fabricated disk-shaped GNIs on HOPG through a top-down two-steps treatment, as shown in Fig. 1. The first preparation step is cyclic H-plasma etching and thermal post-annealing at 1,000 K, producing densed nanopores on the top layer of HOPG (Fig. 1(b)). Following several cycles of H etching, for the second step, the sample was annealed at a higher temperature (1,500 K) which is a bit higher than that in the annealing process of first step. This process results in the formation of
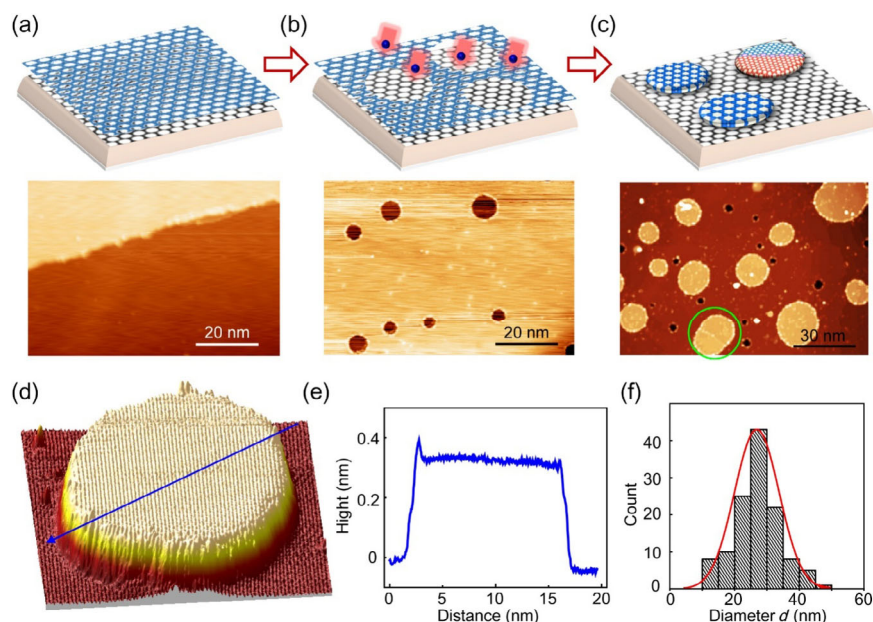

Figure 1 Fabrication of disk-shaped GNIs on HOPG surface. (a)–(c) Illustration of fabrication of GNIs through two-step treatment of HOPG surface and representative large-scale STM images (sample bias: V_s = −3.0 V; tunneling current: I_t = 0.01 nA). The green circle highlights a BC-GNI. (d) Three-dimensional STM topography of a typical as-fabricated high-qualtiy GNI (V_s = −0.2 V; I_t =0. 1 nA). (e) A height profile along the blue arrow in (d), showing that single-layer height of 0.35 nm. (f) Size distribution of the as-grown GNIs, showing that GNIs are 20 to 35 nm in size.

high-quality disk-shaped GNIs (Figs. 1(c) and 1(d)) due to the carbon sublimation and edge reconstructions (see Fig. S1 in the Electronic Supplementary Material (ESM) for detail information). It is worthy to be noticed that there may exist amorphous C and transformation into crystalline in the complex formation process. But we did not observe amorphous C and its transformation into crystalline ones in the STM images of sample after annealing at high temperature (Fig. S1 in the ESM).

The height of GNIs is about 0.35 nm, indicating that all the GNIs are monolayer (Fig. 1(e)). Except for SC-GNI, some GNIs are bicrystal (highlighted by the green circle in Fig. 1(c)). The disk shape of GNI suggests that the GNIs have similar formation energies in all directions under these experimental conditions (with a partial pressure of H_2 gas of 10^{-2} Pa at the temperature of 1,100–1,500 K) [27]. The size of GNIs ranges from 20 to 35 nm (Fig. 1(f)). In addition, the edges of GNIs are expected to be H-terminated due to the hydrogen environment during H-plasma etching. The atomically resolved STM images demonstrate that the protrusions which exist on the edge and interior of GNIs in STM images are attributed from the electronic interference states of edges and defects (Fig. S2 in the ESM).

We next focus on the study of BC-GNIs (Fig. 2(a)). Compared with round shape of SC-BNI, the BC-GNI display an elliptic shape, which indicates that a BC-GNI may originate from merging of two as-formed GNIs during the migration process on the surface at high temperatures (Fig. 2(b) and Fig. S1 in the ESM). On the BC-GNIs, there are one-dimensional line structures (black dot line in Fig. 2(a)) which are interpreted as GB between two adjacent nanodomains. We have checked 300 as-grown GNIs, and 98 of them have GBs. As one or two GBs are found to appear on a GNI, we have found 126 GBs on these GNIs. The fraction of GNIs with GBs is 32.6%, and the density of GBs is 0.42 per island.

The type of GBs is categorized by the tilt angle between the corresponding crystallographic directions in the two domains. In the high-resolution STM image (top in Fig. 2(c)) and corresponding fast Fourier transformation (FFT) patterns (left in Fig. 2(d)) of two domains on BC-GNI, the GBs show a tilt angle of θ = 32° and a periodic pattern with a periodicity of

~ 0.9 nm, which provides a strong suggestion of the possible structure of a 5-7-5-7 GB [16, 25]. For the statistical analysis of as-formed GBs, we obtained the tilt angle of GBs through high-resolution STM images and FFT patterns of hundreds of BC GNIs (see Fig. S3 in the ESM). The histogram (right in Fig. 2(d)) shows that the overwhelming majority is GB with a tilt angle of ~ 32°, that is, 5-7-5-7 GBs, suggesting that the 5-7-5-7 GBs were widely formed during the formation process of GNIs.

The dominance of GBs with 32° tilt angle arises from their formation energy (0.338 eV/Å) being lower than that of other GBs, according to previously published theoretical results [28]. There are two reasons to explain why GBs with 32° tilt angle can be fabricated in this work but mix of various GBs in the literatures: One is that the GBs are formed on graphene domains smaller than 100 nm, which may be generated by the growth mechanism different from the domains in micrometer scale. Another is that the GNIs are produced using a top-down etching method where the merge of GNIs is controlled by the post-annealing temperature while the reported GBs are fabricated by chemical-vapor-deposition methods where the merge of graphene is difficult to be controlled.

We further studied the detailed configurations of two nano-domains abutting GBs with respect to the underlying substrate. The lattice misorientations between two nanodomains and the underlying graphite lattice can be clearly distinguished, respectively, through high-resolution STM images (Fig. S4 in the ESM). The orientation of one domain is the same with the substrate, indicating a normal AB stacking. While, the orientation of another domain is rotated with the substrate by ~ 32°, indicating a twisted stacking. Thus, we conclude that the two domains abutting GBs on BC-GNIs are stacked differently with graphite substrate, that is, AB and twist stacking respectively. Figure 2(c) shows that the STM simulation (middle panel) based on the AB/twist stacking bilayer graphene with 5-7-5-7 GB (bottom panel) agrees well with the STM image (top panel), further confirming the AB/twist stacking orders of two domains and 5-7-5-7 atomic configurations of GBs.

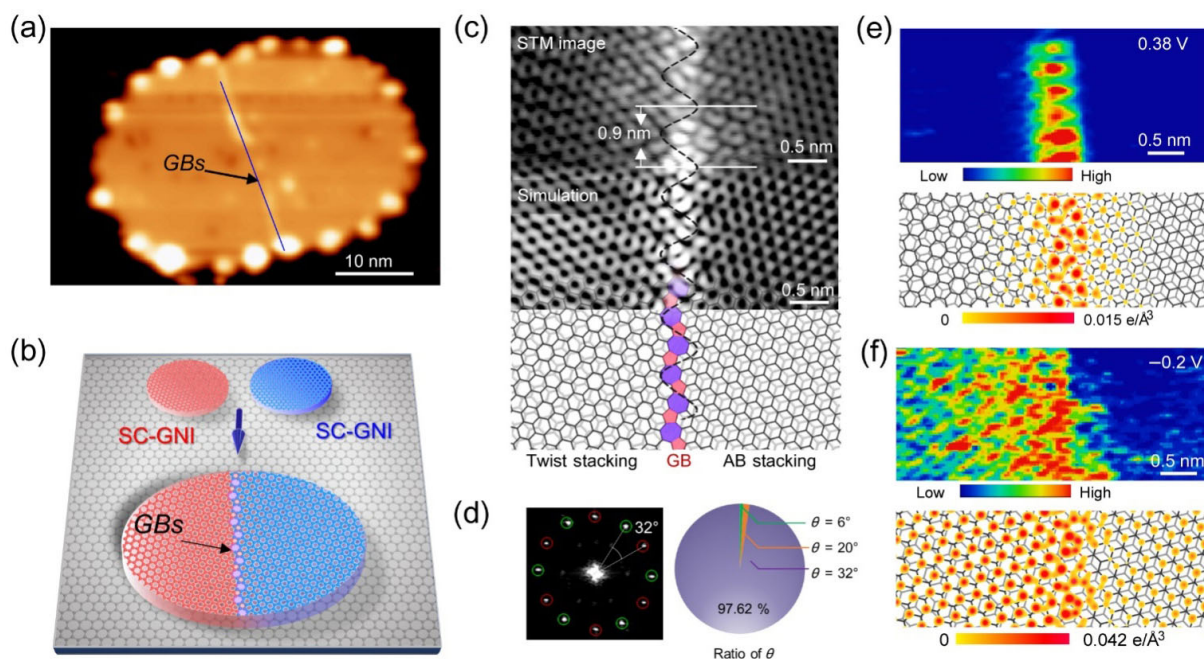At low sample bias, STM images show that the twisted domain

Figure 2 Structures and electronic properties of two nanodomains abutting 5-7-5-7 GBs. (a) Presentative STM image of a BC-GNI, showing an elliptic shape. The black dotted line indicates the GB. (V_s = −2.0 V, I_t = 0.02 nA). (b) Illustration of merging two SC-GNIs into a BC-GNI. (c) STM topography (top), STM simulation (middle), and corresponding atomic configuration (bottom) of AB/twisted stacking nanodomains separated by a 5-7-5-7 GB. (V_s = −0.2 V, I_t = 0.1 nA). (d) Left: FFT pattern corresponding to the STM image in (c), showing a tilt angle of ~ 32° between two domains. Right: Histogram of tilt angles observed on hundreds of GBs, showing that angles of ~ 32° are strongly preferred. (e) Top: dI/dV mapping in the same region in (c) at the bias voltage of 0.38 V, showing that the tunneling conductance along GBs is higher than the one in other regions. Bottom: The calculated electronic-states distribution at 0.38 V. (f) Top: dI/dV mapping in the same region in (c) at the bias voltage of −0.2 V, showing various distribution of density of states between two nanodomains. Bottom: The calculated electronic-states distribution at −0.2 V.

(Twist domain) shows a stronger electronic $(\sqrt{3} \times \sqrt{3})R30°$ interference patterns that are originated from intervalley scattering induced by the GBs than the AB domain does (Fig. S5 in the ESM). In dI/dV spectra obtained on the as-formed GBs with tilt angle of 32° and calculated density of states based on the 5-7-5-7 GBs models, two sharp and intense peaks at −0.42 and 0.38 V (Fig. S5 in the ESM) are spatially localized on the GBs (Fig. 2(e)), indicating that the two states are originated from Van Hove singularities (VHS) [25, 28]. The agreement between dI/dV spectra and calculated density of states further demonstrates that the as-grown GBs are well-defined 5-7-5-7 GBs at the atomic level. Meanwhile, the dI/dV mapping and calculated electronic-states distributions at −0.2 eV shows a stronger intensity on Twist domain (Fig. 2(f)) than that on AB domain. The distinct electronic properties of two domains suggests the formation of a graphene homojunction.

Besides single GB, we fabricated parallelly assembled 5-7-5-7 GBs with various separation distances on a GNI. The separation of the parallel GBs is related to the size of GNIs. Figure 3 show six typical STM images and corresponding atomic models of parallel 5-7-5-7 GBs. We checked the stacking orders of each domains through high-resolution STM images of the GNI edge (Fig. S4 in the ESM). As shown in Figs. 3(a)–3(c), the parallel GBs separate the GNIs into twist/AB/twist stacked domains. The separations are 3.2, 4.9, and 13.3 nm, respectively. As shown in Figs. 3(d)–3(f), the parallel 5-7-5-7 GBs separate the GNIs into domains with AB/twist/AB stacking orders. The separation is 1.5, 2.5 and 4.0 nm, respectively. It is worthy to notice that if the distance between parallel GBs is not far enough, in the middle domain, the electronic $(\sqrt{3} \times \sqrt{3})R30°$ interference pattern from left GB interacts with that from the right GB, resulting in a different electronic structure comparing with that from an isolated GB (Fig. S6 in the ESM). The construction of parallel 5-7-5-7 GBs

provides possibilities to build periodic barriers in graphene-based nanostructures, which may introduce anisotropic behaviors of massless Dirac fermions and chiral tunneling [29]. As various stacking in graphene systems exhibit different electronic properties [30–32], the separated nanodomains with various stacking orders and separation distances provide more degrees of freedom for engineering the electronic structures of graphene. Furthermore, the railroad-track-like structures enable the formation of complex structures, and ultimately be used in graphene-based scalable electronics [23].

To tune the stacking orders and electronic properties of two adjacent nanodomains, we rotated the homojunction through STM manipulation. By approaching the tip closer to the edge of GNI and moving it along one direction, GNIs can be displaced (Fig. S7 in the ESM), rotated (Fig. 4) and even folded [12]. We attribute the lateral motion of GNIs to the weak van der Waals interactions between the STM tip and sample [10]. Figure 4(a) schematically shows the well-defined AB/twist stacking domains with a 5-7-5-7 GB on a homojunction. Briefly, to rotate a GNI, an STM tip is brought close to its edge by reducing the tunneling resistance in the STM junction, followed by moving across the GNI along an out-of-axis direction (green arrow in Fig. 4(a)). Figures 4(a) and 4(b) schematically show the process of rotating a homojunction, where the stacking modes of two domains are tuned from AB/twist into twist/twist. Figures 4(c) and 4(d) show the typical STM images before and after a rotation at an angle of 3.4°. After rotation, moiré patterns were observed on the initial AB stacking regions, due to the twist angle between the homojunction and substrate induced by rotation (Fig. 4(d)). Based on the periodicity of moiré pattern, we calculated the twist angle to be θ = 3.4° (Here θ can also be directly determined by measuring the periodicity d of the moiré pattern (θ = 2arcsin(a/2d), where a is the graphene lattice constant)) which is consistent with the angle of rotation
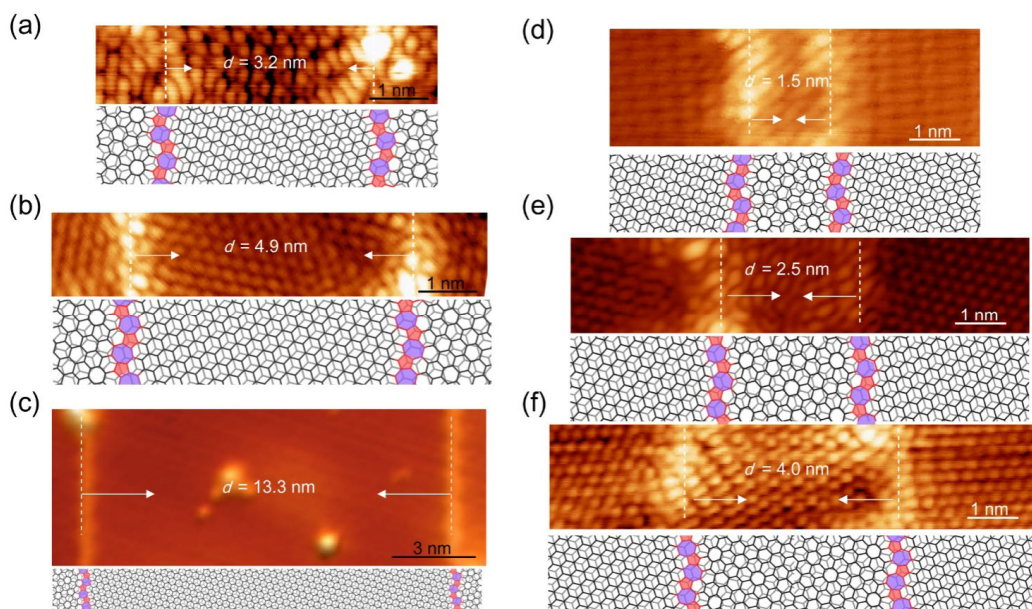
Figure 3 Twist/AB/twist and AB/twist/AB arrays of nanodomains separated by parallel 5-7-5-7 GBs on the graphene homojunction. (a)–(c) STM images and corresponding atomic models showing the formation of twist/AB/twist arrays of parallel 5-7-5-7 GBs in the separation of 3.2 nm (a), 4.9 nm (b), and 13.3 nm (c), respectively ($V_s = -0.2$ V, $I_t = 0.1$ nA). (d)–(f) STM images and corresponding atomic models showing the formation of AB/twist/AB arrays of parallel 5-7-5-7 GBs in the separation of 1.5 nm (d), 2.5 nm (e), and 4.0 nm (f), respectively ($V_s = -0.2$ V, $I_t = 0.1$ nA).
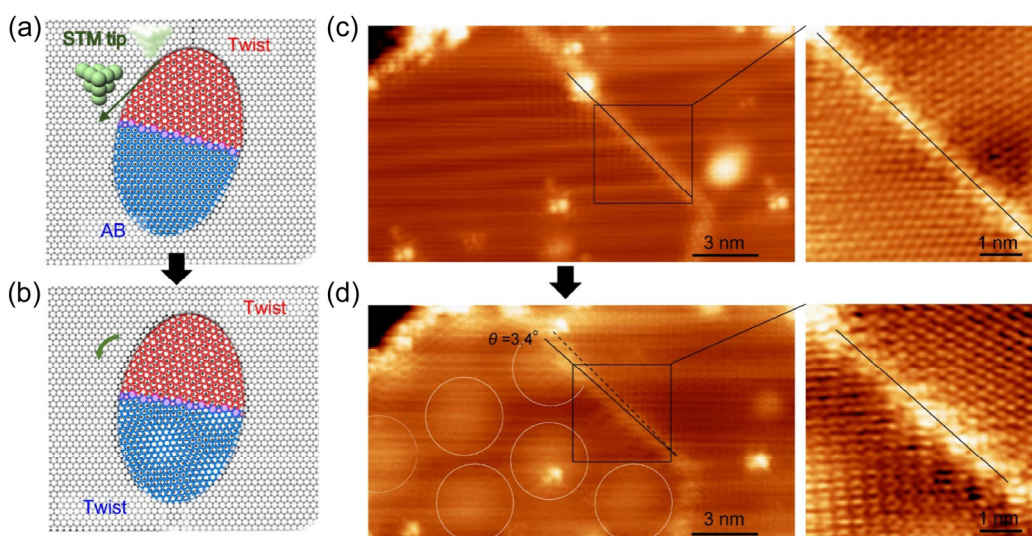

Figure 4 Rotation manipulations of graphene homojunction with 5-7-5-7 GBs. ((a) and (b)) Schematics of a homojunction before (a) and after (b) rotating the islands through moving a STM tip (green balls in (a)) along an out-of-axis direction (green arrow in (a)), showing that the stacking orders of two domains are changed after rotation. (c) Large-scale STM image (left) and high-resolution STM image (right) of homojunction with a 5-7-5-7 GB before rotation. (d) Large-scale STM image (left, $V_s = -1.0$ V, $I_t = 0.01$ nA) and high-resolution STM image (right, $V_s = -0.2$ V, $I_t = 0.1$ nA) of the same homojunction after rotation by 3.4°. The newly-formed moiré patterns are highlighted by white circles. The stacking structures have been changed from AB/twist to twist/twist through rotation.

manipulation. We also found that the distribution of electronic states of the two domains abutting the GB changed significantly compared to the initial one, due to the structural transition from AB/twist to twist/twist stacking. As tiny changes in the stacking orders have been reported to have significant effects in the electronic [30–32], mechanical [33] and chiral [34] properties of the graphene, it stimulates interests to control the configurations and properties of graphene homojunctions in atomic precision. Furthermore, the bilayer or multilayer graphene with magic-angle twisted stacking orders has been reported to exhibit unique properties such as superconductivity [30]. Therefore, the atomically-precise construction of such twisted graphene homojunctions also provides opportunities to study graphene-based superconductor/normal-metal junctions and

related devices [35].

3 Conclusions

We fabricated graphene homojunctions with well-defined 5-7-5-7 GBs on the HOPG surface through a two-step top-down method. The GNIs are in sizes ranging from 20 to 35 nm. Post-annealing step induced the formation of BC-GNIs with GBs by merging of two SC-GNIs. Statistical analysis shows that 95% of the as-formed GBs are 5-7-5-7 GBs, which is further verified by the high-resolution STM/STS and theoretical simulations. Due to different stacking types of the two nanodomains abutting the GB, distinct electronic properties are observed in the two nanodomains, suggesting the formation

of a graphene homojunction. Except for single GB, the 5-7-5-7 GBs arrays can be assembled in a parallel way, connecting domains in alternate AB/twist stacking orders on the homojunction. In addition, we succeeded in rotating the homojunction in a tiny angle via STM tip, in which way to precisely manipulate the stacking modes of the two nanodomains. This work paves a way to fabricate and precisely manipulate lateral junctions consisting of 2D materials with artificially controllable twist angles.

4   Methods

4.1   Sample preparation, STM/STS measurement

The HOPG sample was cleaved in air by tape and subsequently annealed at 900 K in an ultrahigh vacuum (UHV) chamber. The hydrogen-plasma (H-plasma) etching was carried out in a high-vacuum plasma chamber (base pressure of 1×10^{-8} mbar) using a helical, inductively coupled RF plasma source (13.56 MHz at power of 220 W). A gas mixture of H_2 (15%) with Ar (85%) at a pressure of 1×10^{-4} mbar was used. Ion deflection voltage (350 V) was applied. The sample was heated to 750 K during the etching process for maximum etching speed [36]. After H-plasma etching, the sample was transferred to another chamber (base pressure of 1×10^{-10} mbar) and heated using an e-beam heating method (the temperature can be up to 1,500 K). The experiments were carried out in a UHV LT-STM system (Unisoku) with base pressure of 1×10^{-10} mbar at 4.2 K. STM images were acquired in constant-current mode, and all given voltages (V_s) refer to the sample. Differential conductance (dI/dV) spectra were collected by using a lock-in technique with a sinusoidal modulation at a frequency of 973.1 Hz. All STM/STS experiments were performed with electrochemically etched tungsten tips which were calibrated against the surface state of the Au(111) surface before and after spectroscopic measurements.

4.2   First-principles calculations

First-principles calculations based on DFT were performed in a plane-wave formulation with the projector augmented wave method (PAW) [37] as implemented in Vienna ab initio simulation package (VASP) [38, 39]. Local density approximation (LDA) [40] in the form of Perdew–Zunger was adopted for the exchange-correlation functional. The energy cutoff of the plane-wave basis sets was 400 eV. The calculational model for BC graphene was in a 12 nm × 0.9 nm × 2 nm unit cell, designed as a bilayer graphene ribbon containing one-layer pristine graphene and another layer graphene with ordered 5-7-5-7 GB in middle. In the ribbon, one domain is in AB-stacking and the other is in twist-stacking with 32º tilt angle. The ribbon was as wide as ~ 9.3 nm so as to eliminate the effect of the edge states to the boundary. The distance between neighboring ribbons was ~ 2.7 nm. The periodicity along the ribbon is 0.9 nm, which agrees well with the experiment. The thickness of the vacuum layer was 1.7 nm. In structural relaxation, all atoms were relaxed until the force on each atom was less than 0.01 eV/Å. The k-points sampling was 1 × 3 × 1.

Acknowledgements

Electronic Supplementary Material: Supplementary material (detail formation process of GNIs, high-resolution STM images of GNIs and corresponding edges, STM images of two rarely observed GB, representative high-resolution STM image of a GNI edge, STM images of a typical 5-7-5-7 GBs using different sample bias and dI/dV of GBs, STM simulations of parrallel GBs, displacing and rotating of single-crstal GNIs through a STM tip) is available in the online version of this article at https://doi.org/10.1007/s12274-3004-5.

References

[1]   Mishra, S.; Beyer, D.; Eimre, K.; Kezilebieke, S.; Berger, R.; Gröning, O.; Pignedoli, C. A.; Müllen, K.; Liljeroth, P. et al. Topological frustration induces unconventional magnetism in a nanographene. *Nat. Nanotechnol.* **2020**, *15*, 81.

[2]   Cox, J. D.; García de Abajo, F. J. Nonlinear interactions between free electrons and nanographenes. *Nano Lett.* **2020**, *20*, 4792–4800.

[3]   Cox, J. D.; de Abajo, F. J. G. Single-plasmon thermo-optical switching in graphene. *Nano Lett.* **2019**, *19*, 3743–3750.

[4]   Su, J.; Telychko, M.; Hu, P.; Macam, G.; Mutombo, P.; Zhang, H. J.; Bao, Y.; Cheng, F.; Huang, Z. Q.; Qiu, Z. Z. et al. Atomically precise bottom-up synthesis of π-extended [5]triangulene. *Sci. Adv.* **2019**, *5*, eaav7717.

[5]   Chen, H.; Que, Y. D.; Tao, L.; Zhang, Y. Y.; Lin, X.; Xiao, W. D.; Wang, D. F.; Du, S. X.; Pantelides, S. T.; Gao, H. J. Recovery of edge states of graphene nanoislands on an iridium substrate by silicon intercalation. *Nano Res.* **2018**, *11*, 3722–3729.

[6]   Pavliček, N.; Mistry, A.; Majzik, Z.; Moll, N.; Meyer, G.; Fox, D. J.; Gross, L. Synthesis and characterization of triangulene. *Nat. Nanotechnol.* **2017**, *12*, 308–311.

[7]   Leicht, P.; Zielke, L.; Bouvron, S.; Moroni, R.; Voloshina, E.; Hammerschmidt, L.; Dedkov, Y. S.; Fonin, M. *In situ* fabrication of quasi-free-standing epitaxial graphene nanoflakes on gold. *ACS Nano* **2014**, *8*, 3735–3742.

[8]   Phark, S. H.; Borme, J.; Vanegas, A. L.; Corbetta, M.; Sander, D.; Kirschner, J. Direct observation of electron confinement in epitaxial graphene nanoislands. *ACS Nano* **2011**, *5*, 8162–8166.

[9]   Fernández-Rossier, J.; Palacios, J. J. Magnetism in graphene nanoislands. *Phys. Rev. Lett.* **2007**, *99*, 177204.

[10]   Feng, X. F.; Kwon, S.; Park, J. Y.; Salmeron, M. Superlubric sliding of graphene nanoflakes on graphene. *ACS Nano* **2013**, *7*, 1718–1724.

[11]   Zhu, S. Z.; Li, T. Hydrogenation-assisted graphene origami and its application in programmable molecular mass uptake, storage, and release. *ACS Nano* **2014**, *8*, 2864–2872.

[12]   Chen, H.; Zhang, X. L.; Zhang, Y. Y.; Wang, D. F.; Bao, D. L.; Que, Y. D.; Xiao, W. D.; Du, S. X.; Ouyang, M.; Pantelides, S. T. et al. Atomically precise, custom-design origami graphene nanostructures. *Science* **2019**, *365*, 1036–1040.

[13]   Wilson, P. M.; Mbah, G. N.; Smith, T. G.; Schmidt, D.; Lai, R. Y.; Hofmann, T.; Sinitskii, A. Three-dimensional periodic graphene nanostructures. *J. Mater. Chem. C* **2014**, *2*, 1879–1886.

[14]   Heerema, S. J.; Dekker, C. Graphene nanodevices for DNA sequencing. *Nat. Nanotechnol.* **2016**, *11*, 127–136.

[15]   Majee, A. K.; Kommini, A.; Aksamija, Z. Electronic transport and thermopower in 2D and 3D heterostructures—A theory perspective. *Ann. Phys.* **2019**, *531*, 1800510.

[16]   Yazyev, O. V.; Louie, S. G. Electronic transport in polycrystalline graphene. *Nat. Mater.* **2010**, *9*, 806–809.

[17]   Gunlycke, D.; White, C. T. Graphene valley filter using a line defect. *Phys. Rev. Lett.* **2011**, *106*, 136806.

[18]   Chen, J. H.; Autès, G.; Alem, N.; Gargiulo, F.; Gautam, A.; Linck, M.; Kisielowski, C.; Yazyev, O. V.; Louie, S. G.; Zettl, A. Controlled growth of a line defect in graphene and implications for gate-tunable valley filtering. *Phys. Rev. B* **2014**, *89*, 121407(R).

[19] Xu, J.; Yuan, G. W.; Zhu, Q.; Wang, J. W.; Tang, S.; Gao, L. B. Enhancing the strength of graphene by a denser grain boundary. *ACS Nano* **2018**, *12*, 4529–4535.

[20] Alexandre, S. S.; Lúcio, A. D.; Neto, A. H. C.; Nunes, R. W. Correlated magnetic states in extended one-dimensional defects in graphene. *Nano Lett*. **2012**, *12*, 5097–5102.

[21] Kou, L. Z.; Tang, C.; Guo, W. L.; Chen, C. F. Tunable magnetism in strained graphene with topological line defect. *ACS Nano* **2011**, *5*, 1012–1017.

[22] Wu, H. C.; Chaika, A. N.; Hsu, M. C.; Huang, T. W.; Abid, M.; Abid, M.; Aristov, V. Y.; Molodtsova, O. V.; Babenkov, S. V.; Niu, Y. R. et al. Large positive in-plane magnetoresistance induced by localized states at nanodomain boundaries in graphene. *Nat. Commun*. **2017**, *8*, 14453.

[23] Gunlycke, D.; Vasudevan, S.; White, C. T. Confinement, transport gap, and valley polarization in graphene from two parallel decorated line defects. *Nano Lett*. **2013**, *13*, 259–263.

[24] Biró, L. P.; Lambin, P. Grain boundaries in graphene grown by chemical vapor deposition. *New J. Phys*. **2013**, *15*, 035024.

[25] Tison, Y.; Lagoute, J.; Repain, V.; Chacon, C.; Girard, Y.; Joucken, F.; Sporken, R.; Gargiulo, F.; Yazyev, O. V.; Rousset, S. Grain boundaries in graphene on SiC(0001) substrate. *Nano Lett*. **2014**, *14*, 6382–6386.

[26] Yang, B.; Xu, H.; Lu, J.; Loh, K. P. Periodic grain boundaries formed by thermal reconstruction of polycrystalline graphene film. *J. Am. Chem. Soc*. **2014**, *136*, 12041–12046.

[27] Chen, Y. B.; Sun, J. Y.; Gao, J. F.; Du, F.; Han, Q.; Nie, Y. F.; Chen, Z. L.; Bachmatiuk, A.; Priydarshi, M. K.; Ma, D. L. et al. Growing uniform graphene disks and films on molten glass for heating devices and cell culture. *Adv. Mater*. **2015**, *27*, 7839–7846.

[28] Yazyev, O. V.; Louie, S. G. Topological defects in graphene: Dislocations and grain boundaries. *Phys. Rev. B* **2010**, *81*, 195420.

[29] Katsnelson, M. I.; Novoselov, K. S.; Geim, A. K. Chiral tunnelling and the klein paradox in graphene. *Nat. Phys*. **2006**, *2*, 620–625.

[30] Cao, Y.; Fatemi, V.; Fang, S. A.; Watanabe, K.; Taniguchi, T.; Kaxiras, E.; Jarillo-Herrero, P. Unconventional superconductivity in magic-angle graphene superlattices. *Nature* **2018**, *556*, 43–50.

[31] Cao, Y.; Fatemi, V.; Demir, A.; Fang, S. A.; Tomarken, S. L.; Luo, J. Y.; Sanchez-Yamagishi, J. D.; Watanabe, K.; Taniguchi, T.; Kaxiras, E. et al. Correlated insulator behaviour at half-filling in magic-angle graphene superlattices. *Nature* **2018**, *556*, 80–84.

[32] Sharpe, A. L.; Fox, E. J.; Barnard, A. W.; Finney, J.; Watanabe, K.; Taniguchi, T.; Kastner, M. A.; Goldhaber-Gordon, D. Emergent ferromagnetism near three-quarters filling in twisted bilayer graphene. *Science* **2019**, *365*, 605–608.

[33] Lin, J. H.; Fang, W. J.; Zhou, W.; Lupini, A. R.; Idrobo, J. C.; Kong, J.; Pennycook, S. J.; Pantelides, S. T. AC/AB stacking boundaries in bilayer graphene. *Nano Lett*. **2013**, *13*, 3262–3268.

[34] Kim, C. J.; Sánchez-Castillo, A.; Ziegler, Z.; Ogawa, Y.; Noguez, C.; Park, J. Chiral atomically thin films. *Nat. Nanotechnol*. **2016**, *11*, 520–524.

[35] Hikino, S.; Yunoki, S. Anomalous enhancement of spin Hall conductivity in a superconductor/normal-metal junction. *Phys. Rev. B* **2011**, *84*, 020512(R).

[36] Yang, R.; Zhang, L. C.; Wang, Y.; Shi, Z. W.; Shi, D. X.; Gao, H. J.; Wang, E. G.; Zhang, G. Y. An anisotropic etching effect in the graphene basal plane. *Adv. Mater*. **2010**, *22*, 4014–4019.

[37] Kresse, G.; Joubert, D. From ultrasoft pseudopotentials to the projector augmented-wave method. *Phys. Rev. B* **1999**, *59*, 1758–1775.

[38] Vanderbilt, D. Soft self-consistent pseudopotentials in a generalized eigenvalue formalism. *Phys. Rev. B* **1990**, *41*, 7892–7895.

[39] Kresse, G.; Furthmüller, J. Efficient iterative schemes for *ab initio* total-energy calculations using a plane-wave basis set. *Phys. Rev. B* **1996**, *54*, 11169–11186.

[40] Perdew, J. P.; Zunger, A. Self-interaction correction to density-functional approximations for many-electron systems. *Phys. Rev. B* **1981**, *23*, 5048–5079.